Highlighting the impact of blocking monolayers on DNA electrochemical sensors. Theoretical and experimental investigations under flow conditions

Martina Freisa, Claire Poujouly, Isabelle Le Potier, Thi Hong Nhung Dinh, Laurent Couraud, David Bouville, Catherine Sella, Laurent Thouin, Jean Gamby

Highlighting the impact of blocking monolayers on DNA electrochemical sensors. Theoretical and experimental investigations under flow conditions

Martina Freisa,[a] Claire Poujouly,[a] Isabelle Le Potier,[a] Thi Hong Nhung Dinh,[a] Laurent Couraud,[a] David Bouville,[a] Catherine Sella,[b] Laurent Thouin,[b,*] and Jean Gamby [a,*]

[a] *Université Paris-Saclay, CNRS, Centre de Nanosciences et de Nanotechnologies, 91120, Palaiseau, France*

[b] *PASTEUR, Département de chimie, Ecole normale supérieure, PSL University, Sorbonne Université, CNRS, 75005, Paris, France*

*** Corresponding authors:** laurent.thouin@ens.psl.eu, jean.gamby@c2n.upsaclay.fr

Abstract

A model is proposed to account for the influence of electrode surface modifications in electrochemical DNA sensors operating under flow conditions. With blocking self-assembled monolayers of double-stranded DNA, the performance of the electrochemical transduction signal in the presence of a redox mediator is generally attributed to the rate of long-range electron transfer or to the screening effects of the monolayers due to negatively charged DNA. The originality of this model is here to only consider the influence of non-linear mass transport at the free-remaining sites. The model was tested for the detection of microRNAs (21 nucleotides) by implementing microchannel electrodes in the presence of an equimolar mixture of $Fe(CN)_6^{3-}$ / $Fe(CN)_6^{4-}$. Two operating conditions leading to distinct monolayer structures were investigated using Pt and Au electrodes. The model successfully simulated the voltammograms confirming the apparent decrease in the signal transduction kinetics due to altered mass transport. These results were supported by measurements in electrochemical impedance spectroscopy.

Keywords: SAMs; RNA; microfluidics; amperometry; EIS.

1. Introduction

Biosensors are powerful tools that convert a biological or chemical response into a measurable signal [1–4]. In recent years, biosensors gained enormous attention for the detection and analysis of biological molecules and chemical processes [3,5–7]. Devices with embedded biosensors cover a wide range of applications, including diagnostic tools, environmental monitoring of pollutants, detection of pathogens in food, and bioprocess controlling [8]. Among several types of sensors, electrochemical biosensors offer high sensitivity, simplicity, affordability, and rapidity [9]. Moreover, they can be easily miniaturized and integrated into microfluidics devices, permitting low sample consumption, easy liquid handling and higher performance.[9,10]. For this reason, the field of electrochemical tools has experienced significant attraction [11]. Electrochemical biosensors rely on a biological recognition element, such as enzymes, nucleic acids, proteins, etc., which specifically interacts with the target analyte [12,13]The signal transduction enabled by the electrochemical cell translates the biorecognition into an electrical signal, permitting the detection and quantification of the analyte under investigation [14].

Electrochemical biosensors for nucleic acid detection are also encouraging tools for overcoming traditional techniques, which are usually time-consuming [15], expensive, and require specialized equipment [16,17]. Indeed, nucleic acids (NAs), including DNAs, RNAs, circulating tumor DNA, and microRNAs, play a crucial role in biological processes [18]. Numerous nucleic acids have been identified as biomarkers, which is really promising to guarantee early detection for a multitude of diseases, such as cancers, cardiovascular diseases, and bacterial infections [19–24]. Moreover, NA detection also finds application in forensic science and the food industry [25–28]. The biorecognition in NA detectors is typically based on the hybridization event between the analyte targets and complementary probes immobilized at the electrode surface [29–37]. After this event, signal transduction is induced through specific electrochemical oxidations or reductions at the electrode. Electrochemical detection of NA offers advantages since it allows direct transduction without an amplification step with PCR [29–34].

In this field, electroanalytical performance of DNA biosensors is determinant [18,38–40]. The evolution of the detection limits of these biosensors shows that many breakthroughs have been achieved for a variety of transduction pathways. The lowest detection limits reported in the literature reached the femtomolar level for biosensors based on catalyzed long-range electron transfer [31,35–37], or the attomolar level for those coupled

with nanoplatform sensing amplification [3,41–45]. In particular, these biosensors allow the detection of a single mismatch at room temperature, which remains a major topic in this field [36,46]. However, as with other pathways, there are still significant issues to be addressed to improve the performance in sensitivity and selectivity [2,12,34,43,47,48]. A deep understanding of the processes remains challenging due to the complexity of the mechanisms involved, particularly with sensors based on self-assembled monolayers (SAMs) architectures. Indeed, the transduction signal results from the alteration of the redox processes and the modulation of their kinetics after probe immobilization and target hybridization. For long-range electron transfer, variations are often attributed to modulations of charge transfer mechanisms coupled with screening effects of SAMs due to negatively charged DNAs. In this case, it cannot be excluded that SAMs may also alter the diffusion processes towards the electrode surface and therefore modulate the overall transduction kinetics. It appears all the more important to take this property into account if these sensors are integrated into miniaturized devices in flow conditions, where mass transport under confinement ultimately determines the performance. In this context, we wanted to address further the performance of electrochemical biosensors based on blocking monolayers in microfluidic devices. In the field of DNA sensors, distinguishing the restricted electroactive area from the overall decrease in electron transfer rate still remains a dilemma preventing the complete description of the processes involved in signal transduction. Macroscopically, electron transfer kinetics decreases upon modification of electrode surfaces. Standard electrochemical techniques measure the overall electrochemical current which is a spatial average of the electron rate across the surface. They rely on variations in peak currents in cyclic voltammetry (CV) and charge transfer resistance in electrochemical impedance spectroscopy (EIS) [12,29,32,33,36,37,42,44,46,49–58]. Therefore, fundamentally, these techniques cannot distinguish whether this is due to either restricted electroactive area or an overall decrease of the electron transfer rate. Several mathematical models have been developed to analyze these data and identify the underlying mechanisms resulting from surface modifications. In the following, we introduced a simple model to illustrate the situation where the apparent kinetics of the transduction signal is only controlled by the accessibility of the electrode through holes within the monolayers. This model was tested without long-range electron transfer by detecting miR-30b and miR-122 (21 nucleotides) under two distinct operating conditions, with Pt and Au microchannel electrodes, respectively. In these cases, the presence of defects or pinholes is necessary because no electron transfer between the redox probes and the electrode via

tunneling through 21-nucleotide molecular barriers is expected. After immobilization and hybridization of the single-stranded RNA, detections were achieved by implementing both CV and EIS measurements using a two-electrode cell configuration, in the presence of an equimolar mixture of the redox mediators $Fe(CN)_6^{3-}$ and $Fe(CN)_6^{4-}$. Data obtained in CV were analyzed to assess the coverage surface ratio of the electrode surface according to the model. Comparisons with EIS measurements were carried out in order to confirm the alteration of mass transport due to the SAM properties.

2. Experimental

2.1. Microfluidic chips

The microfluidic devices were fabricated using clean room facilities. The chip comprised a polydimethylsiloxane (PDMS) cover for the microfluidic channels and a glass substrate that supports the electrochemical cells (Fig. 1). In all the devices, the electrochemical system included two microband electrodes comprising upstream a working electrode (WE) of 30 μm width and 300 μm length, and downstream a counter electrode (CE) of 2 mm width and 300 μm length [36,59]. These electrodes were separated by a gap distance of 100 μm.

The fabrication process was implemented with 4-inch glass wafers by combining photolithography, metal deposition, and lift-off procedures. The negative lithography was accomplished by using the AZ5214 photoresist (Microchemicals), followed by an oxygen plasma etching for 30 seconds. 10 nm of Ti was evaporated as an adhesion layer prior to 100 nm of platinum or gold, depending on the device under study. Afterward, the lift-off was carried out in an ultrasound acetone bath for 10 min, followed by a rinsing step with isopropanol. Finally, the wafer was cut into several chips.

The PDMS cover was realized by molding PDMS (RTV 615, Neyco) on a 4-inch silicon wafer. The master mold was fabricated by lithography using SU-8 2002 (Microchemicals) and SU-8 2050 (Microchemicals) photoresists. The height of the resulting microchannels was measured by profilometry and evaluated equal to 60 μm. A mixing ratio of 1:10 between curing agent and silicone elastomer was used for the preparation of PDMS mixture. This mixture was poured on the master mold, set under vacuum for about 1 hour, and then placed for 4 hours in an oven at 60°C. Finally, the PDMS layer was removed and diced with a blade. For each device, the inlet and outlet of the microchannel were punched with a 0.5 mm needle.

To complete the chip preparation, the glass substrate was bonded with the PDMS cover by air plasma bonding, and the resulting assembly was placed for 1 hour in an oven at 60°C.

Finally, two pairs (WE,CE) of platinum electrodes in individual microchannels were electrochemically studied, as well as three pairs (WE,CE) of gold electrodes. They were named PT1, PT2, AU1, AU2 and AU3, respectively (*see* Table 1 for experimental conditions applied).

2.2. Chemicals

The ssDNA probes and targets designed for miR-30b and miR-122 detection were composed of 21 nucleotides and were purchased from Eurogentec, ssDNA was preferred to RNA due to higher stability and easily storage. They were purified by reverse-phase HPLC purification and delivered in a dried format. The probes were thiol-labeled with a 5' (-SH) C6 modification. They mimicked the complementary target sequence.

For Au-electrode functionalization (to detect miR-122 sequence: 5′—GCAGTGTGACAATGGTGTTTG—3′), the immobilization of probes was accomplished with a 10^{-7} M ssDNA concentration in NaCl. For Pt-electrode functionalization (to detect miR-30b sequence: 5'-UGUAAACAUCCUACACUCAGCU-3'), the solution comprised a mixture of 10^{-6} M probes and 10^{-4} M of 6-Mercaptohexanol (MCH, Sigma Aldric) in NaCl. With both Au and Pt electrodes, the probes immobilization was carried out in static condition for 2 hours. Additionally, the complementary targets were diluted in NaCl, and the hybridization process was performed in static conditions for 30 minutes. In all electrolytes, NaCl concentration was 0.5 M to maintain the DNA structure stability. High salinity permits the neutralization of negative charges of the phosphate backbone and prevents DNA condensation. The pH of the synthetic solution was about 5.

2.3. Instrumentation and measurements

For both the Pt and Au microdevices, the configuration and geometry were the same (Fig. 1). A two-electrode cell configuration was implemented with a high area ratio between the CE and WE electrodes, such as S_{CE} / S_{WE} = 67 [36,59]. An equimolar mixture of the redox mediators $Fe(CN)_6^{3-}$ and $Fe(CN)_6^{4-}$ was here mandatory in order to set the rest potential around 0V in the two-electrode cell configuration. Note that this strategy was demonstrated and discussed elsewhere [31,36]. Experiments were thus carried out in a 0.5 M NaCl solution

containing $Fe(CN)_6^{3-}$ and $Fe(CN)_6^{4-}$ at equal concentrations, *i.e.*, 20 mM and 3 mM for the Pt and Au microdevices, respectively.

A flow rate of 0.5 $\mu L.s^{-1}$ was imposed using a NEMESYS programmable syringe pump. According to the cross section geometry of the channel and the width of the WE, the regime was fully convective (*i.e.*, Levich regime) [59] with an average flow velocity of 2.78 $cm.s^{-1}$.

The EIS measurements were performed using a Biologic Potentiostat (SP300). A 10 mV sinusoidal voltage perturbation for frequencies *f* between 1 MHz to 100 mHz was superimposed on the 0 V equilibrium potential. The comparison between the perturbation signal and the response defined the complex impedance $Z = \Re e\{Z\} + j\Im m\{Z\}$ at given *f*.

In linear sweep voltammetry, measurements were also performed using the Biologic Potentiostat (SP300). The potential was swept in the [-0.2,+0.2] V potential range at 20 mVs^{-1} scan rate. The voltammograms were recorded after each electrode-surface modification and then compared with each other.

2.4. Numerical Simulations

The electrode responses in linear sweep voltammetry were simulated using COMSOL Multiphysics 6.0. The formulation of the problem was based on those already described [59,60]. The mass transport equation was solved numerically at the microband electrodes under laminar flow condition. Since the width of the microchannel was much larger than the height, and since the electrode length was equal to the microchannel width, the problem could be drastically simplified by only considering a two-dimensional space for calculations. The electrochemical reaction was supposed to be controlled both by the electron transfer rate and by the mass transport. For linear sweep voltammetry, the Butler-Volmer and the mass transport equations were solved numerically by finite elements in association with appropriate boundary conditions. All the conditions and protocol used to fit the experimental voltammograms are reported in Supporting Information.

SIMAD software, initially developed at the LISE laboratory, was used for simulating the EIS spectra.

3. Formulation of the problem and modelling

In the field of DNA sensors, distinguishing the restricted electroactive area from the overall decrease in electron transfer rate still remains the main dilemma preventing the complete description of processes involved in signal

transduction. In the following, a model was designed to account for the alteration of the mass transport above an electrode whose surface is partially modified and blocked by the immobilization of NA probes (*i.e*., by the formation of a thiol-labeled ss-DNA) and then by the targets (*i.e*., after hybridization of the SAMs by the complementary ss-DNA). Indeed, the partial coverage of the electrode due to the formation of SAMs, is supposed to generate a large number of microscopic active sites. In this case, the partial blocking of the electrode with respect to electron transfer can be evaluated by the accessibility to the surface of redox mediators added in solution.

Starting from these expectations, a model can be derived from one that was previously developed to explain voltammetry at spatially heterogeneous electrodes [60]. This model has opened the way to the investigation of a large variety of issues in electrochemistry. In the present case, the approach is addressed to the case of microchannel electrodes operating under convective regimes, and more specifically, to the issue of microchannel electrodes modified by SAMs with DNA-labelled thiols. Under such conditions, mass transport exalted at the electrode surface, should lead to nonlinear effects of diffusion-convection on the amperometric responses of the sensors. Considering the geometry of the microfluidic device used, some 3D schematic views are provided in Fig. 2A, left column, to illustrate the electrode interface foreseen during the three different steps: (i) initially, the surface of the bare electrode is fully active; (ii) after modification by the thiol-labeled ss-DNA, the electrode surface is partially covered by the SAM, leading to the formation of holes which operate as active sites of average size w_i; (iii) after hybridization, due to the formation of ds-DNA, some holes are filled by the steric hindrance of the double strands and/or masked following the reorganization of the monolayers. This leads to a decrease in the number of holes and to a decrease in the average size w_i, In both steps, the surface coverage ratio decreases.

In the modelling, several hypotheses were thus made to simplify the formulation of the problem in a 2D space (Fig. 2A, right column):

- The surface coverage ratio in 2D space remains unchanged since holes are randomly distributed.
- The cross coupling between active sites (*i.e*., overlap between diffusion-convection layers) is negligible since high surface coverage leads to large distances between active sites.
- The active sites can be merged together in N microbands of width w_i.
- The electrode-surface coverage ratio is defined as:

$$\theta = 1 - \frac{N\ w_i}{w} \quad (1)$$

The electron transfer rate constant k_0 of the redox probe at active sites is supposed to not vary after functionalization and hybridization of the electrodes. Therefore, depending on only two main parameters (N,w_i), the operation of the actives sites can be easily simulated as microband electrodes in a 2D space (Fig. 2B), ultimately allowing the determination of θ.

Initially, the surface of the bare electrode is fully active and the electrode experiences well-known regimes of a microband electrode under flow conditions (Fig. 2B step i). These regimes depend on the geometry of the device (electrode width w, channel height h) and flow velocity [61]. As expected in this case, the resulting voltammogram displays a sigmoidal shape characteristic of a steady-state regime with a limiting current i^L. In the absence of ohmic drop, the slope of the voltammogram close to the equilibrium potential is related to the standard electron transfer rate k_0 of the redox species. As the electron transfer rate k_0 is constant in the successive steps, the generation of small active sites should induce non-linear effects of mass transport on the ensuing voltammograms (Fig. 2B, steps ii and iii) according to the original predictions established with partially blocked electrodes [60],

Therefore, following all the above assumptions, each active site operates independently and can be modelled as single sites. Regarding these assumptions, the model we propose is simple and based on solving in linear sweep voltammetry the mass transport equation under flow condition, while keeping constant the electron transfer rate at the active sites. A unique and minimal cell configuration is considered both for bare electrodes of size w or for modified electrodes with active sites of average size w_i (Fig. 2C). The procedure for simulating and fitting the voltammograms is detailed in Supporting Information.

4. Results and discussion

4.1. Experimental and simulated voltammograms

In order to validate the model, the synthetic solutions described in experimental section were employed and introduced in the microdevices. Note that the use of complex matrices with different pH was under the scope of this study. Note also that since the detection protocol did not involve a redox intercalator as catalyst, transduction was not expected to occur here via long-range electron transfer. Indeed, no methylene blue (MB)

or other DNA redox intercalators were added in order to mediate such electron transfer [36]. At this level, alteration of the voltammograms are supposed to be only controlled by the convective mass transport and by the coverage surface ratio of the electrodes, according to the successive steps leading to surface modifications: (i) without any modification (*i.e.*, bare electrode), (ii) after functionalization by the probes (*i.e.*, with thiol-labeled ss-DNA), and (iii) after hybridization with increasing concentrations of the targets. Fig. 3 shows some examples of voltammograms recorded at a Pt microchannel electrode (PT1 electrode) after each step. As expected, the voltammograms exhibit the characteristic shape of steady-state voltammograms centered at the axis origin, due to the implementation of the two-electrode cell configuration *(i.e.*, without a reference electrode). The use of an equimolar mixtures of redox mediators $Fe(CN)_6^{3-}$ and $Fe(CN)_6^{4-}$ leads to the apparent symmetry observed on each side of the voltammograms. The cathodic and anodic limiting currents are almost identical. Little differences in current amplitude can be noticed but they can be easily attributed to the discrepancy between the diffusion coefficients of $Fe(CN)_6^{3-}$ and $Fe(CN)_6^{4-}$. The symmetry observed for all the voltammograms here clearly demonstrate identical electrochemical processes in oxidation and reduction. However, the electrode modifications achieved after each step led to an alteration of the apparent kinetics. Indeed, slopes at low overpotentials and limiting currents at higher potentials decreased concomitantly with electrode modification.

The model described previously was applied in order to check whether these behaviors were consistent with the initial assumptions. Simulations were carried out so as to reproduce the experimental voltammograms according to a procedure described in detail in Supporting Information. The electron transfer rate k_0 was first evaluated by fitting the bare-electrode voltammogram. After electrode modifications, the coverage surface ratio θ_{volta} was then estimated by adjusting the parameters (N,w_i) while keeping constant the k_0 value. In such a case, θ_{volta} (*see* Eq.1) was defined as:

$$\theta_{\text{volta}} = 1 - \frac{N_{\text{volta}}\ w_i}{w} \tag{2}$$

$$\text{with } N_{\text{volta}} = \frac{i_{\text{exp}}^{\text{L}}}{i_{\text{sim}}^{\text{L}}} \tag{3}$$

$$\text{and } i_{\text{sim}}^{\text{L}} = -FlD\int_0^{wi}\left(\frac{\partial c}{\partial y}\right)_{y=0} dx \tag{4}$$

i_{sim}^{L} and i_{exp}^{L} are the simulated and experimental limiting currents monitored at -0.2 V on the plateau of the steady-state voltammogram.

As shown in Fig. 3, fairly good agreement was obtained in all the experiments between simulated and experimental voltammograms, up to the precision of the experimental measurements and the fitting procedure. These results demonstrated at first glance the validity of the model. The non-linear effects of mass transport thus explain the evolution of the voltammograms after each step, without introduction a variable apparent rate constant k_0. The set of parameters (k_0, $w_i N_{volta}$) used for each fit and the resulting θ_{volta} were summarized in Table 1, together with the experimental conditions. Note on the one hand, that the coverage surface ratio θ_{volta} was deduced from the fits of current amplitude. On the other hand, the size w_i of active sites was deduced from the slope of voltammogram around the equilibrium potential. As an illustration, Fig. 4A shows values of slope simulated as a function of w_i for several k_0 values investigated here. With bare electrode, no coverage surface ratio was introduced. In this case, the electrode surface in Fig. 3 was found initially to be fully active as confirmed by the ratio $N_{volta} = 0.99$ obtained from the experimental i_{exp} and simulated i_{sim} currents. In addition, the value of k_0 used to fit this voltammogram was consistent with a quasi-reversible system with $k_0 = 0.03$ cm s^{-1}. After functionalization and hybridization, the covered surface ratio θ_{volta} increased from 0.87 after functionalization to 0.96 after hybridization. Accordingly, the sizes w_i of the active sites were much smaller than the nominal size w of the electrode. w_i decreased from 0.8 to 0.4 μm.

All the behaviors and characteristics in Fig. 3 were also consistent with other experiments conducted with Pt and Au electrodes (*see* PT2, AU1, AU2, and AU3 electrodes in Figs. S1-4 in supporting information). The corresponding data set (k_0, w_i, N_{volta}) deduced from the fits was also reported in Table 1 for comparison. Despite the different experimental conditions and protocols employed between these experiments, the same trends were observed within the experimental uncertainties. Due to electrostatic repulsions within the duplex, the negatively charged $Fe(CN)_6^{3-}$ and $Fe(CN)_6^{4-}$ species can only penetrate the layer towards active sites that remain accessible. Note that the incorporation of MCH for the modification of Pt electrodes aimed to better structure the monolayer and to avoid disordered orientations of DNA strands due to the strong affinity of adenosine and guanine for platinum [62]. MCH was not required for the modification of Au electrodes because the thiol functions strongly adsorb on gold. Thus, the good correlation observed between experimental and simulated voltammograms attests that electrode modifications under disparate conditions indeed modify the

mass transport of redox mediators and the overall kinetics of transduction signal. This was observed whatever the protocol used for the modification of the electrodes and therefore whatever the structure of the monolayers which generates the active sites.

4.2. Experimental and simulated EIS

The EIS experiments were also carried out under flow conditions in an equimolar solution of $Fe(CN)_6^{3-}$ and $Fe(CN)_6^{4-}$. The potential was set at the equilibrium potential to ensure proper functioning of the DNA sensor and to accurately determine the charge transfer resistance (*see* below). For each step, the impedance data was simulated using a modified Randles circuit (Fig. 5) adapted from those traditionally used to model a coating organic layer acting on surface as paint or blocking layer [63,64]. The asymptotic limit of the real part Z_R at low frequency domain (LF) was thus the sum of (i) the global electrolyte resistance R_e, (ii) the local electrolyte resistance in surface and/ or SAMs defects R'_e, (iii) the charge transfer resistance R_{ct}, and (iv) the convection-diffusion resistance R_D (*i.e.* when $Z_{D,f\to 0}$). Two different capacitances were considered, with C_b corresponding to the blocking layer capacitance, and C_{dl} representing the double layer capacitance. This latter was modelled with a constant-phase element (CPE, with Q_{dl} and α_{dl} parameters) in order to take into account a 2-D distribution of current and potential electrode [63]. It could be turned into an equivalent frequency-independent capacitance $C_{dl,eq}$ calculated by the use of formula given by Brug *et. al*. [65]:

$$C_{\mathrm{dl,eq}} = \left[Q_{dl}\left(\frac{1}{R_\mathrm{e}+R'_e}+\frac{1}{R_\mathrm{ct}}\right)^{\alpha-1}\right]^{\frac{1}{\alpha}} \quad (5)$$

In this equation, note that R_{ct} is considered because its value can be comparable to the sum $(R_\mathrm{e} + R'_e)$ under certain conditions.

The R_{ct} bare values were also used to estimate the heterogeneous charge transfer rate constant k_0 by applying Eq. 6 as:

$$k_0 = \frac{RT}{\mathrm{F}^2 S R_{\mathrm{ct},\eta\to 0} C^0} \quad (6)$$

where, T is the temperature (293.16 K), R the molar gas constant (8.31446 J.mol^{-1}.K^{-1}), F the Faraday constant (96485.3 C.mol^{-1}), S the bare surface area of Pt and Au electrodes (9 10^{-5} cm^2), $R_{ct,\eta\to 0}$, the charge transfer resistance (between 1.7 kΩ and 47.2 kΩ, respectively) at the zero overpotential, and C^0 the concentration

(mol.m^{-3}). In parallel to experiments in voltammetry, the resulting coverage surface ratio θ_{EIS} were calculated by normalizing the apparent $R_{ct,ap}$ value against R_{ct} value initially deduced on bare electrode, as follows:

$$\theta_{EIS} = 1 - \frac{R_{ct,bare}}{R_{ct},ap} \quad (7)$$

The results obtained from the PT1 electrode are displayed as Nyquist plots in Fig. 6 and for the other Pt and Au electrodes in Figs. S5-8. All raw parameters found by the fit procedure with the electrical equivalent circuit described above were reported in Table S1. Only a constraint in the high frequency domain (HF) was imposed for *Re* due to the consistent use of the same supporting electrolyte in all experiments. As observed, the $C_{dl,eq}$ values were consistent with the expected values for bare Pt and Au electrodes, *i.e.*, between 25 µF.cm^{-2} and 3 µF.cm^{-2}. The k_0 values ranged between 8.7 10^{-2} cm.s^{-1} and 2.1 10^{-2} cm.s^{-1} in accordance with the quasi reversible $Fe(CN)_6^{4-}/Fe(CN)_6^{3-}$ system. In Fig. 6, for the PT1 electrode, the following observations could be drawn: (i) R_e value, which depends on the electrolyte conductivity and the electrode size, was found as a constant around 2kΩ, (ii) R_{ct} value drastically increased from bare to hybridization step, from 1,7 kΩ to 113.6 kΩ, respectively, and consequently, (iii) the covered surface ratio θ_{EIS} varied from 0.90 to 0.98. The results were quite similar for PT2 electrode (Fig. S5), while for AU1, AU2, and AU3 electrodes (Figs. S6-8), higher R_{ct} values were found while keeping the same tendency.

4.3. Comparison between data from voltammetry and EIS

Only the relevant parameters for all the electrodes investigated were listed in Table 1. The comparison between the coverage surface ratios θ_{EIS} and θ_{volta} was straightforward. Indeed, a very good agreement was overall noticed between θ_{EIS} and θ_{volta} whatever the Pt or Au electrodes. Fig. 4B displays such a correlation by plotting θ_{EIS} as a function of θ_{volta}. Compared to Au electrodes, a weaker correlation with Pt electrodes was nevertheless observed. This could be partly explained by lower discrepancies between R_e and R_{ct} at bare Pt electrodes. Indeed, the prevalence of R_e in such a case should impact the shapes of the voltammograms, and therefore their fits by the model. This necessarily leads to an underestimation of the charge transfer rate constant k_0 at bare electrodes as well as an underestimation of the coverage surface ratio θ_{volta} at the modified electrodes (*see* Table 1). These differences could be also ascribed to the differences in experimental conditions used for functionalization and hybridization at Pt and Au electrodes.

However, within these uncertainties, and from disparate conditions of electrode modifications, the results validate the present model. The initial assumption of an apparent decrease in the signal transduction kinetics is fully consistent with the alteration of mass transport by the partial electrode coverage. This can be easily observed on voltammograms by the concomitant decrease of slopes and current amplitude. This is also supported by considering the net change on the second loop in EIS spectra from which the couple of values (R_D, τ_D) can be derived. Indeed, in the lower frequency domain R_D is characteristic of the convective-diffusion impedance (f->0), while τ_D is the time to diffusion on the electrode surface. For PT1 electrode, the couple (R_D, τ_D) increases as R_e' and θ_{EIS} (Table S1). This is fully in agreement with the decrease of w observed in Table 1.

5. Conclusion

In this work, we wanted to address further the performance of electrochemical biosensors based on blocking monolayers in microfluidic devices. In the field of DNA sensors, distinguishing the restricted electroactive area from the overall decrease in electron transfer rate is still a dilemma preventing the complete description of the processes. Moreover, classical electrochemical techniques cannot distinguish whether the apparent kinetics of the transduction signal is due to restricted electroactive area or to an overall decrease of the electron transfer rate. We thus developed a simple model to illustrate the situation where the signal is only controlled by the alteration of mass transport of redox mediators through the holes created within the monolayers. This model was successfully tested under two separate operating conditions for detecting miR-30b or miR-122 (21 nucleotides) either at Pt or Au microchannel electrodes, respectively. Under these conditions, the model perfectly showed that the decrease of the apparent kinetics was not related to the charge transfer rate constant k_0 but rather to a gradual alteration of the mass transport in the vicinity of micro structured interfaces. These results were confirmed by EIS measurements. Therefore, the practical and theoretical findings presented in this paper are expected to contribute significantly to enhancing the electroanalytical performance of DNA biosensors. The model presented here could be improved to apply to the case of long-range electron transfer. These results should also pave the way for better detecting absorbed non-electroactive macromolecules forming blocking monolayers on electroactive surfaces.

ACKNOWLEDGMENTS

The authors thank the DIMELEC project ANR-19-CE09-0016 for funding and RENATECH clean room facilities at C2N, Palaiseau, France. This work was supported in parts by CNRS UMR 8640, ENS (Ecole normale superieure), PSL University and Sorbonne Université. M.F. and C.P. thanks doctoral school "Electrical, Optical, Bio-Physics and Engineering" (ED575) and Paris-Saclay University for PhD grants. We wish to thank Jérémy Le Gall, and Djamila Kechkeche for fruitful discussions.

References

[1] V. Naresh, N. Lee, A review on biosensors and recent development of nanostructured materials-enabled biosensors, Sensors (Switzerland) 21 (2021) 1–35. https://doi.org/10.3390/s21041109.

[2] J. Qin, W. Wang, L. Gao, S.Q. Yao, Emerging biosensing and transducing techniques for potential applications in point-of-care diagnostics, Chem Sci 13 (2022). https://doi.org/10.1039/d1sc06269g.

[3] S.P. Usha, H. Manoharan, R. Deshmukh, R. Álvarez-Diduk, E. Calucho, V.V.R. Sai, A. Merkoçi, Attomolar analyte sensing techniques (AttoSens): A review on a decade of progress on chemical and biosensing nanoplatforms, Chem Soc Rev 50 (2021). https://doi.org/10.1039/d1cs00137j.

[4] A. Clifford, J. Das, H. Yousefi, A. Mahmud, J.B. Chen, S.O. Kelley, Strategies for Biomolecular Analysis and Continuous Physiological Monitoring, J Am Chem Soc 143 (2021). https://doi.org/10.1021/jacs.0c13138.

[5] A. Hasan, M. Nurunnabi, M. Morshed, A. Paul, A. Polini, T. Kuila, M. Al Hariri, Y.K. Lee, A.A. Jaffa, Recent advances in application of biosensors in tissue engineering, Biomed Res Int 2014 (2014). https://doi.org/10.1155/2014/307519.

[6] K. Hsieh, B.S. Ferguson, M. Eisenstein, K.W. Plaxco, H.T. Soh, Integrated Electrochemical Microsystems for Genetic Detection of Pathogens at the Point of Care, Acc Chem Res 48 (2015). https://doi.org/10.1021/ar500456w.

[7] S.S. Mahshid, S. Camiré, F. Ricci, A. Vallée-Bélisle, A Highly Selective Electrochemical DNA-Based Sensor That Employs Steric Hindrance Effects to Detect Proteins Directly in Whole Blood, J Am Chem Soc 137 (2015). https://doi.org/10.1021/jacs.5b04942.

[8] M.S. Sumitha, T.S. Xavier, Recent advances in electrochemical biosensors – A brief review, Hybrid Advances 2 (2023). https://doi.org/10.1016/j.hybadv.2023.100023.

[9] D.G. Rackus, M.H. Shamsi, A.R. Wheeler, Electrochemistry, biosensors and microfluidics: a convergence of fields, Chem Soc Rev 44 (2015) 5320–5340. https://doi.org/10.1039/c4cs00369a.

[10] D. Grieshaber, R. MacKenzie, J. Vörös, E. Reimhult, Electrochemical biosensors - Sensor principles and architectures, Sensors 8 (2008). https://doi.org/10.3390/s8031400.

[11] A. Singh, A. Sharma, A. Ahmed, A.K. Sundramoorthy, H. Furukawa, S. Arya, A. Khosla, Recent advances in electrochemical biosensors: Applications, challenges, and future scope, Biosensors (Basel) 11 (2021). https://doi.org/10.3390/bios11090336.

[12] A.E. Radi, J.L. Acero Sánchez, E. Baldrich, C.K. O'Sullivan, Reagentless, reusable, ultrasensitive electrochemical molecular beacon aptasensor, J Am Chem Soc 128 (2006). https://doi.org/10.1021/ja053121d.

[13] H.A.M. Faria, V. Zucolotto, Label-free electrochemical DNA biosensor for zika virus identification, Biosens Bioelectron 131 (2019). https://doi.org/10.1016/j.bios.2019.02.018.

[14] R.P. Johnson, J.A. Richardson, T. Brown, P.N. Bartlett, A label-free, electrochemical SERS-based assay for detection of DNA hybridization and discrimination of mutations, J Am Chem Soc 134 (2012). https://doi.org/10.1021/ja304663t.

[15] Y. Yu, H.Y.Y. Nyein, W. Gao, A. Javey, Flexible Electrochemical Bioelectronics: The Rise of In Situ Bioanalysis, Advanced Materials 32 (2020). https://doi.org/10.1002/adma.201902083.

[16] T. Tian, J. Wang, X. Zhou, A review: MicroRNA detection methods, Org Biomol Chem 13 (2015) 2226–2238. https://doi.org/10.1039/c4ob02104e.

[17] J. Ye, M. Xu, X. Tian, S. Cai, S. Zeng, Research advances in the detection of miRNA, J Pharm Anal 9 (2019) 217–226. https://doi.org/10.1016/j.jpha.2019.05.004.

[18] J. Jiang, H. Wu, Y. Su, Y. Liang, B. Shu, C. Zhang, Electrochemical Cloth-Based DNA Sensors (ECDSs): A New Class of Electrochemical Gene Sensors, Anal Chem 92 (2020). https://doi.org/10.1021/acs.analchem.0c00669.

[19] J. Wang, J. Chen, S. Sen, MicroRNA as Biomarkers and Diagnostics, J Cell Physiol 231 (2016) 25–30. https://doi.org/10.1002/jcp.25056.

[20] V. Vlassov, P. Laktionov, E. Rykova, Circulating Nucleic Acids as a Potential Source for Cancer Biomarkers, Curr Mol Med 10 (2010). https://doi.org/10.2174/156652410790963295.

[21] F. Momen-Heravi, S.J. Getting, S.A. Moschos, Extracellular vesicles and their nucleic acids for biomarker discovery, Pharmacol Ther 192 (2018). https://doi.org/10.1016/j.pharmthera.2018.08.002.

[22] B. Ralla, C. Stephan, S. Meller, D. Dietrich, G. Kristiansen, K. Jung, Nucleic acid-based biomarkers in body fluids of patients with urologic malignancies, Crit Rev Clin Lab Sci 51 (2014). https://doi.org/10.3109/10408363.2014.914888.

[23] T. Gilboa, P.M. Garden, L. Cohen, Single-molecule analysis of nucleic acid biomarkers – A review, Anal Chim Acta 1115 (2020). https://doi.org/10.1016/j.aca.2020.03.001.

[24] S.R. Shin, Y.S. Zhang, D.J. Kim, A. Manbohi, H. Avci, A. Silvestri, J. Aleman, N. Hu, T. Kilic, W. Keung, M. Righi, P. Assawes, H.A. Alhadrami, R.A. Li, M.R. Dokmeci, A. Khademhosseini, Aptamer-Based Microfluidic Electrochemical Biosensor for Monitoring Cell-Secreted Trace Cardiac Biomarkers, Anal Chem 88 (2016). https://doi.org/10.1021/acs.analchem.6b02028.

[25] E.K. Hanson, J. Ballantyne, Highly specific mRNA biomarkers for the identification of vaginal secretions in sexual assault investigations, Science and Justice 53 (2013). https://doi.org/10.1016/j.scijus.2012.03.007.

[26] E.K. Hanson, H. Lubenow, J. Ballantyne, Identification of forensically relevant body fluids using a panel of differentially expressed microRNAs, Anal Biochem 387 (2009) 303–314. https://doi.org/10.1016/j.ab.2009.01.037.

[27] B. Bahadur, M.V. Rajam, L. Sahijram, K. V. Krishnamurthy, Plant biology and biotechnology: Volume II: Plant genomics and biotechnology, Plant Biology and Biotechnology: Volume II: Plant Genomics and Biotechnology II (2015) 1–768. https://doi.org/10.1007/978-81-322-2283-5.

[28] P. Rani, V.R. Yenuganti, S. Shandilya, S.K. Onteru, D. Singh, miRNAs: The hidden bioactive component of milk, Trends Food Sci Technol 65 (2017) 94–102. https://doi.org/10.1016/j.tifs.2017.05.007.

[29] C. Tersch, F. Lisdat, Label-free detection of protein-DNA interactions using electrochemical impedance spectroscopy, Electrochim Acta 56 (2011). https://doi.org/10.1016/j.electacta.2011.06.063.

[30] J.C. Cunningham, N.J. Brenes, R.M. Crooks, Paper electrochemical device for detection of DNA and thrombin by target-induced conformational switching, Anal Chem 86 (2014). https://doi.org/10.1021/ac501438y.

[31] M.C. Horny, M. Lazerges, J.M. Siaugue, A. Pallandre, D. Rose, F. Bedioui, C. Deslouis, A.M. Haghiri-Gosnet, J. Gamby, Electrochemical DNA biosensors based on long-range electron transfer: Investigating the efficiency of a fluidic channel microelectrode compared to an ultramicroelectrode in a two-electrode setup, Lab Chip 16 (2016). https://doi.org/10.1039/c6lc00869k.

[32] N. Falcone, Z. She, C. Chen, B. Dong, D. Yi, H.B. Kraatz, Demonstration of a tailorable and PCR-free detection of: Enterococcus DNA isolated from soil samples, Analytical Methods 9 (2017). https://doi.org/10.1039/c6ay03309a.

[33] N.S. Zambry, M.S. Awang, K.K. Beh, H.H. Hamzah, Y. Bustami, G.A. Obande, M.F. Khalid, M. Ozsoz, A.A. Manaf, I. Aziah, A label-free electrochemical DNA biosensor used a printed circuit board gold electrode (PCBGE) to detect SARS-CoV-2 without amplification, Lab Chip 23 (2023). https://doi.org/10.1039/d2lc01159j.

[34] L.C. Lopes, A. Santos, P.R. Bueno, An outlook on electrochemical approaches for molecular diagnostics assays and discussions on the limitations of miniaturized technologies for point-of-care devices, Sensors and Actuators Reports 4 (2022). https://doi.org/10.1016/j.snr.2022.100087.

[35] J.D. Slinker, N.B. Muren, A.A. Gorodetsky, J.K. Barton, Multiplexed DNA-modified electrodes, J Am Chem Soc 132 (2010). https://doi.org/10.1021/ja909915m.

[36] C. Poujouly, J. Le Gall, M. Freisa, D. Kechkeche, D. Bouville, J. Khemir, P. Gonzalez-Losada, J. Gamby, Microfluidic Chip for the Electrochemical Detection of MicroRNAs: Methylene Blue Increasing the Specificity of the Biosensor, Front Chem 10 (2022). https://doi.org/10.3389/fchem.2022.868909.

[37] N. Basu, T.H. Ho, F.X. Guillon, Y. Zhang, P. Bigey, B. Navakanta, F. Bedioui, M. Lazerges, Coupling Electrochemical Adsorption and Long-range Electron Transfer: Label-free DNA Mismatch Detection with Ultramicroelectrode (UME), Electroanalysis 31 (2019). https://doi.org/10.1002/elan.201900357.

[38] H.L.L. Yu, A. Maslova, I.M. Hsing, Rational Design of Electrochemical DNA Biosensors for Point-of-Care Applications, ChemElectroChem 4 (2017). https://doi.org/10.1002/celc.201600756.

[39] M. Trotter, N. Borst, R. Thewes, F. von Stetten, Review: Electrochemical DNA sensing – Principles, commercial systems, and applications, Biosens Bioelectron 154 (2020). https://doi.org/10.1016/j.bios.2020.112069.

[40] X. Hai, Y. Li, C. Zhu, W. Song, J. Cao, S. Bi, DNA-based label-free electrochemical biosensors: From principles to applications, TrAC - Trends in Analytical Chemistry 133 (2020). https://doi.org/10.1016/j.trac.2020.116098.

[41] T.G. Drummond, M.G. Hill, J.K. Barton, Electrochemical DNA sensors, Nat Biotechnol 21 (2003) 1192–1199. https://doi.org/10.1038/nbt873.

[42] P. Williamson, P. Piskunen, H. Ijäs, A. Butterworth, V. Linko, D.K. Corrigan, Signal Amplification in Electrochemical DNA Biosensors Using Target-Capturing DNA Origami Tiles, ACS Sens 8 (2023). https://doi.org/10.1021/acssensors.2c02469.

[43] L. Soleymani, Z. Fang, E.H. Sargent, S.O. Kelley, Programming the detection limits of biosensors through controlled nanostructuring, Nat Nanotechnol 4 (2009). https://doi.org/10.1038/nnano.2009.276.

[44] A.M. Nowicka, M. Fau, T. Rapecki, M. Donten, Polypyrrole-Au Nanoparticles Composite as Suitable Platform for DNA Biosensor with Electrochemical Impedance Spectroscopy Detection, Electrochim Acta 140 (2014). https://doi.org/10.1016/j.electacta.2014.03.187.

[45] A.T. Sage, J.D. Besant, B. Lam, E.H. Sargent, S.O. Kelley, Ultrasensitive electrochemical biomolecular detection using nanostructured microelectrodes, Acc Chem Res 47 (2014). https://doi.org/10.1021/ar500130m.

[46] F. Patolsky, A. Lichtenstein, I. Willner, Electronic transduction of DNA sensing processes on surfaces: Amplification of DNA detection and analysis of single-base mismatches by tagged liposomes, J Am Chem Soc 123 (2001). https://doi.org/10.1021/ja0036256.

[47] T.M. Squires, R.J. Messinger, S.R. Manalis, Making it stick: Convection, reaction and diffusion in surface-based biosensors, Nat Biotechnol 26 (2008). https://doi.org/10.1038/nbt1388.

[48] J. Wu, H. Liu, W. Chen, B. Ma, H. Ju, Device integration of electrochemical biosensors, Nature Reviews Bioengineering 1 (2023). https://doi.org/10.1038/s44222-023-00032-w.

[49] Y.T. Long, C.Z. Li, H.B. Kraatz, J.S. Lee, AC impedance spectroscopy of native DNA and M-DNA, Biophys J 84 (2003). https://doi.org/10.1016/S0006-3495(03)70046-0.

[50] F. Lucarelli, G. Marrazza, M. Mascini, Enzyme-based impedimetric detection of PCR products using oligonucleotide-modified screen-printed gold electrodes, in: Biosens Bioelectron, 2005. https://doi.org/10.1016/j.bios.2004.08.025.

[51] E.P. Randviir, C.E. Banks, Electrochemical impedance spectroscopy: An overview of bioanalytical applications, Analytical Methods 5 (2013). https://doi.org/10.1039/c3ay26476a.

[52] G. Yang, J. Cao, L. Li, R.K. Rana, J.J. Zhu, Carboxymethyl chitosan-functionalized graphene for label-free electrochemical cytosensing, Carbon N Y 51 (2013). https://doi.org/10.1016/j.carbon.2012.08.020.

[53] G. Congur, E. Eksin, A. Erdem, Impedimetric Detection of microRNA at Graphene Oxide Modified Sensors, Electrochim Acta 172 (2015). https://doi.org/10.1016/j.electacta.2015.03.210.

[54] L. Tang, Y. Wang, J. Li, The graphene/nucleic acid nanobiointerface, Chem Soc Rev 44 (2015). https://doi.org/10.1039/c4cs00519h.

[55] A.R. Cardoso, F.T.C. Moreira, R. Fernandes, M.G.F. Sales, Novel and simple electrochemical biosensor monitoring attomolar levels of miRNA-155 in breast cancer, Biosens Bioelectron 80 (2016). https://doi.org/10.1016/j.bios.2016.02.035.

[56] L. Ribovski, V. Zucolotto, B.C. Janegitz, A label-free electrochemical DNA sensor to identify breast cancer susceptibility, Microchemical Journal 133 (2017). https://doi.org/10.1016/j.microc.2017.03.011.

[57] S.J. Kang, S. Kim, K. Lee, I.-S. Shin, Y.-R. Kim, Tunable Electrochemical Grafting of Diazonium for Highly Sensitive Impedimetric DNA Sensor, J Electrochem Soc 167 (2020). https://doi.org/10.1149/1945-7111/ab8ce8.

[58] E.B. Bahadir, M.K. Sezgintürk, A review on impedimetric biosensors, Artif Cells Nanomed Biotechnol 44 (2016). https://doi.org/10.3109/21691401.2014.942456.

[59] P. Gonzalez-Losada, M. Freisa, C. Poujouly, J. Gamby, An Integrated Multiple Electrochemical miRNA Sensing System Embedded into a Microfluidic Chip, Biosensors (Basel) 12 (2022). https://doi.org/10.3390/bios12030145.

[60] C. Amatore, J.M. Savéant, D. Tessier, Charge transfer at partially blocked surfaces. A model for the case of microscopic active and inactive sites, Journal of Electroanalytical Chemistry 147 (1983). https://doi.org/10.1016/S0022-0728(83)80055-2.

[61] C. Amatore, N. Da Mota, C. Sella, L. Thouin, Theory and experiments of transport at channel microband electrodes under laminar flows. 1. Steady-state regimes at a single electrode, Anal Chem 79 (2007). https://doi.org/10.1021/ac070971y.

[62] W. Zhou, J. Ding, J. Liu, A platinum shell for ultraslow ligand exchange: unmodified DNA adsorbing more stably on platinum than thiol and dithiol on gold, Chemical Communications 51 (2015) 12084–12087. https://doi.org/10.1039/c5cc04340a.

[63] I.C.P. Margarit-Mattos, EIS and organic coatings performance: Revisiting some key points, Electrochim Acta 354 (2020). https://doi.org/10.1016/j.electacta.2020.136725.

[64] L. Beaunier, I. Epelboin, J.C. Lestrade, H. Takenouti, Etude electrochimique, et par microscopie electronique a balayage, du fer recouvert de peinture, Surface Technology 4 (1976). https://doi.org/10.1016/0376-4583(76)90036-4.

[65] G.J. Brug, A.L.G. van den Eeden, M. Sluyters-Rehbach, J.H. Sluyters, The analysis of electrode impedances complicated by the presence of a constant phase element, Journal of Electroanalytical Chemistry 176 (1984). https://doi.org/10.1016/S0022-0728(84)80324-1.

Experimental conditions					Simulations of voltammograms				Simulations of EIS spectra			
electrodes		C_{probe} / M	C_{target} / M	C_{FeII} and C_{FeIII} / M	k_0 / cm.s^{-1}	w *or* w_i / µm	N_{volta}	θ_{volta}	R_e/ Ω	$R_{ct,ap}$/ kΩ	θ_{EIS}	χ^2 (%)
PT1	bare	-	-	0.02	0.028	30.0	0.99	0.00	2034	1.72	0.00	1.15
	funct	10^{-6}	-		0.028	0.8	4.83	0.87		18.6	0.90	0.97
	hyb_1	-	10^{-14}		0.028	0.6	3.44	0.93		64.9	0.97	0.82
	hyb_2		10^{-10}		0.028	0.5	2.97	0.95		102	0.98	0.83
	hyb_3		10^{-6}		0.028	0.4	2.92	0.96		114	0.98	0.80
PT2	bare	-	-	0.02	0.027	30.0	1.01	0.00	2034	1.70	0.00	1.03
	funct	10^{-6}	-		0.027	1.0	3.54	0.89		34.1	0.94	0.86
	hyb_1	-	10^{-14}		0.027	0.6	2.78	0.94		79.1	0.97	0.94
	hyb_2		10^{-10}		0.027	0.5	2.54	0.96		129	0.98	0.86
	hyb_3		10^{-6}		0.027	0.5	2.07	0.97		159	0.99	0.88
AU1	bare	-	-	0.003	0.028	30.0	0.89	0.00	2000	33.3	0.00	1.10
	funct	10^{-7}	-		0.028	0.8	6.11	0.84		249	0.87	1.00
	hyb	-	10^{-6}		0.028	0.3	8.57	0.91		463	0.93	0.93
AU2	bare	-	-	0.003	0.021	30.0	0.93	0.00	2000	47.3	0.00	0.59
	funct	10^{-7}	-		0.021	1.3	4.92	0.78		255	0.82	0.74
	hyb	-	10^{-6}		0.021	0.5	7.74	0.88		349	0.86	0.79
AU3	bare	-	-	0.003	0.033	30	0.98	0.00	2000	29.0	0.00	0.92
	funct	10^{-7}	-		0.033	0.6	6.88	0.87		248	0.88	0.91
	hyb	-	10^{-6}		0.033	0.3	9.11	0.91		461	0.94	0.79

Table 1: Comparison between data obtained from simulations of voltammograms and from electrochemical impedance spectra: h = 60 µm, L = 300 µm, D^{FeIII} = 7.2 10^{-6} cm^2.s^{-1}, D^{FeII} = 6.5 10^{-6} cm^2.s^{-1}, E^0 = 0 V, α = 0.5, flow rate 0.5 µL.s^{-1}. The values of the resulting χ^2 statistic were obtained with errors of fitted values σ=0.01, for frequency ranging from 1 MHz to 100 mHz.

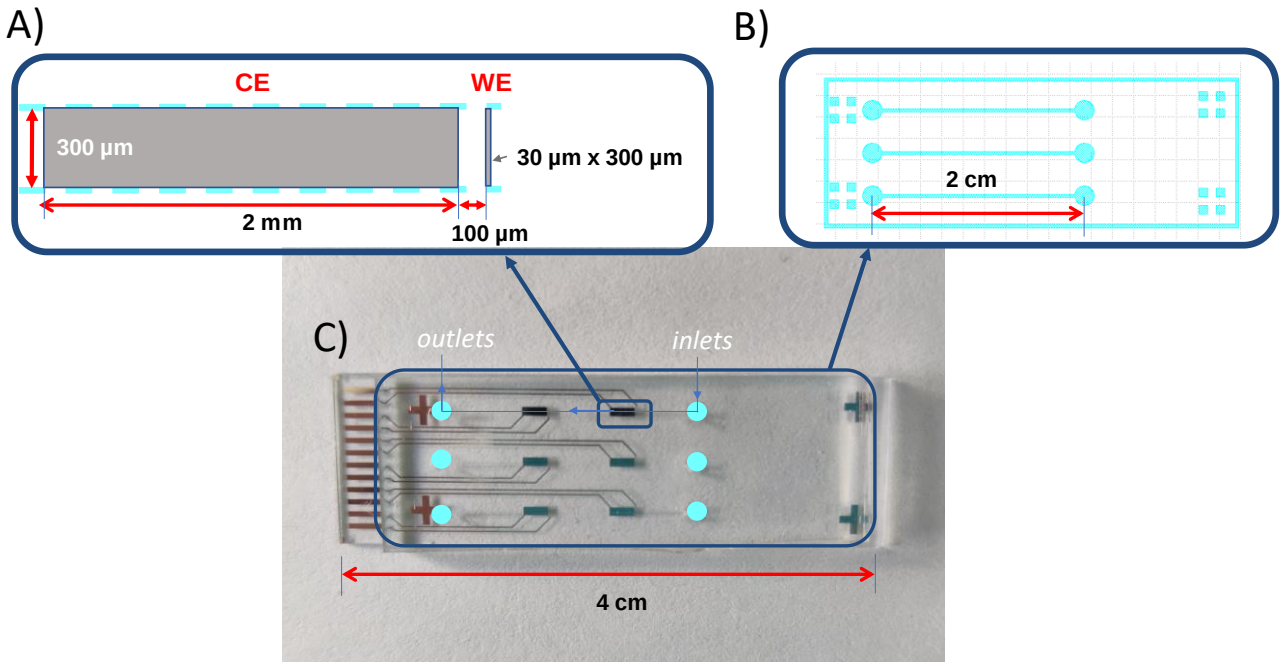

Fig.1: Design and characteristics of the microfluidic devices. A) Dimensions of one pair of electrodes (CE and WE) in a microchannel. B) PDMS mold for three PDMS channels replication. C) Exemple of a final device comprising three pairs of electrodes (WE and CE).

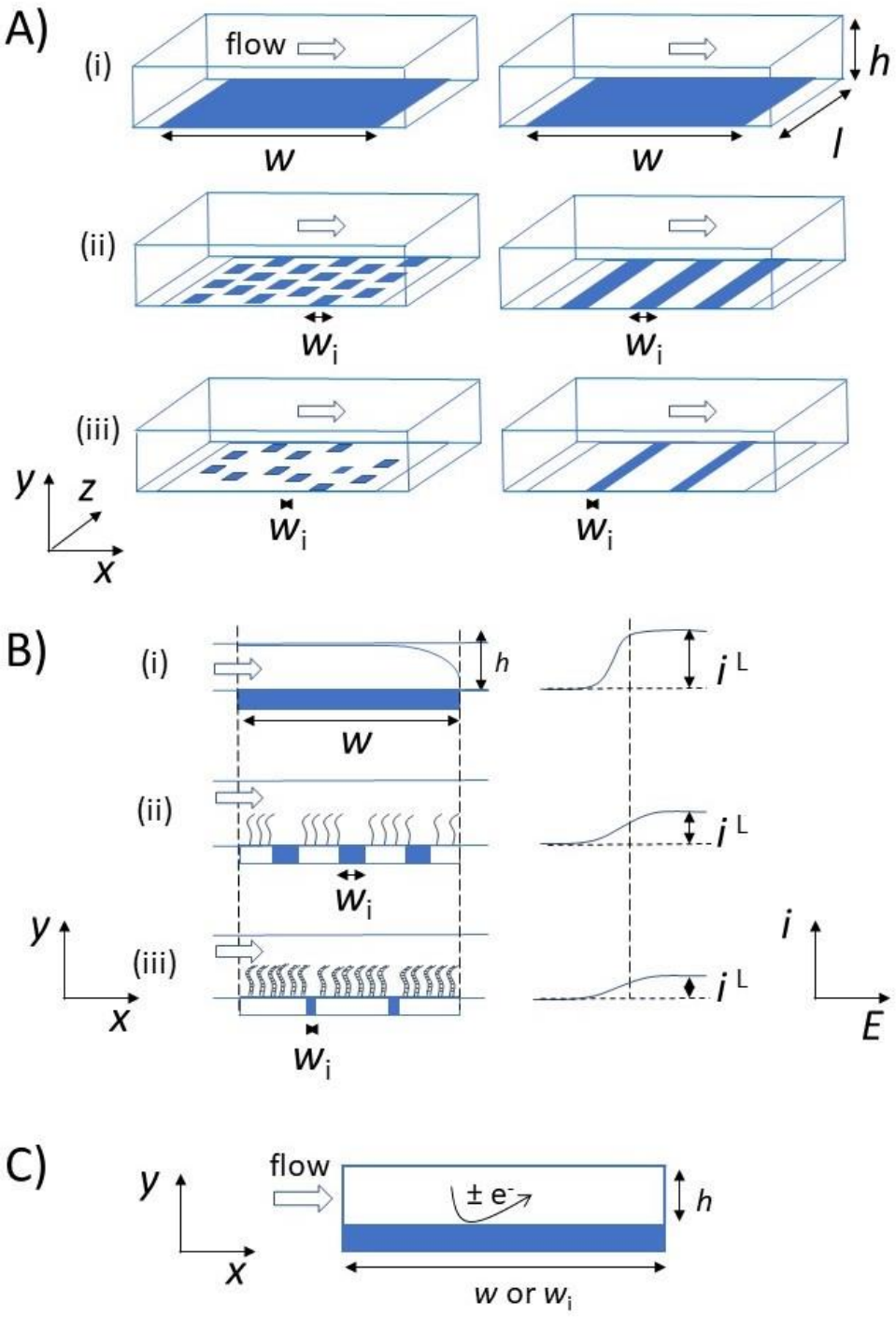

Fig. 2: Modeling of the working electrode interface after the three successive steps. A) 3D views of the working electrode interface with random distribution of electrode active sites (left column) and corresponding modelling (right column). B) 2D views of the electrode interface (left) and corresponding shapes of steady-state voltammograms (right). C) Cell configuration used for 2D simulations. In (A-C), (i) bare electrode (blue area), (ii) electrode after functionalization with probes, and (iii) electrode after hybridization with targets. Electrode width *w*, microchannel width *l,* microchannel height *h,* size of electrode active sites w_i, and limiting current i^L.

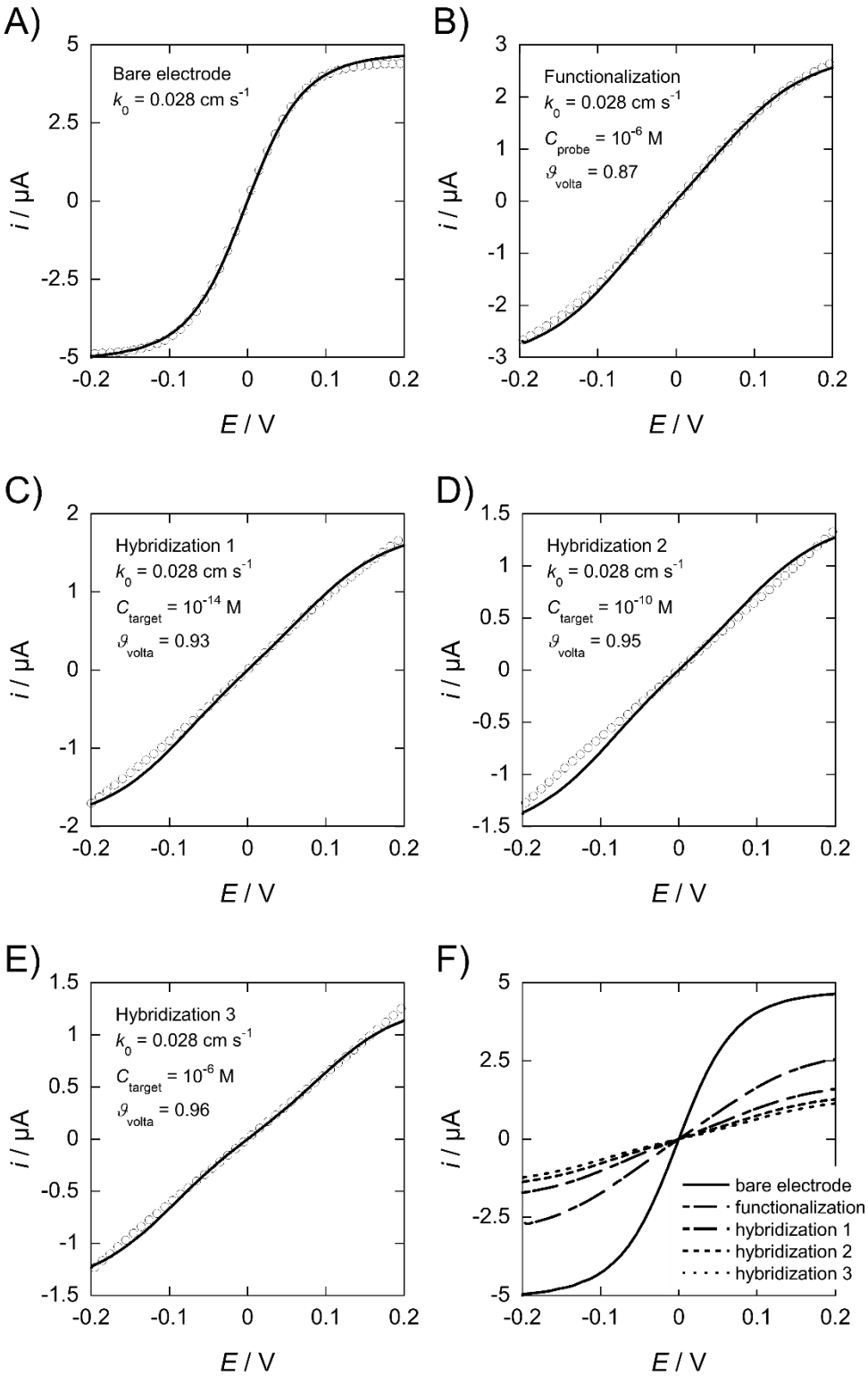

Fig. 3: Experimental (symbols) and simulated (lines) voltammograms on platinum electrode PT1 in solutions containing 20 mM $Fe(CN)_6^{3-}$ and 20 mM $Fe(CN)_6^{4-}$. A) Bare electrode. B) After functionalization with probes. C-E) After hybridization with increasing concentrations of targets. F) Simulated voltammograms in (A-E). See Table 1 for experimental conditions and fitting parameters.

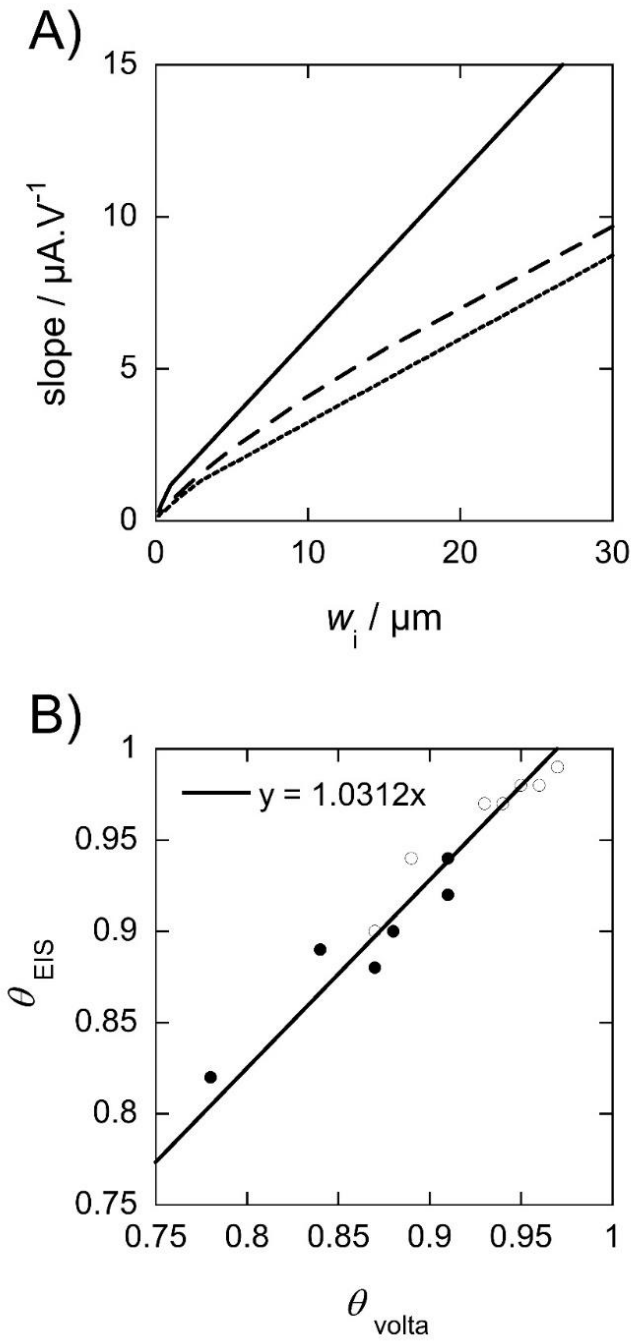

Fig. 4: A) Simulated slopes of voltammograms in the range [-0.05, +0.05] V as a function of the size w of active surface. k_0 = 0.033 cm.s^{-1}(solid lines) k_0 = 0.028 cm.s^{-1} (dashed line) and k_0 = 0.021 cm.s^{-1} (dotted line). B) Comparison between coverage surface ratio θ_{EIS} estimated from impedance electrochemical spectra and coverage surface ratio θ_{volta} evaluated from voltammograms. Data obtained with gold electrodes (open circles) and platinum electrodes (full circles) from Table 1.

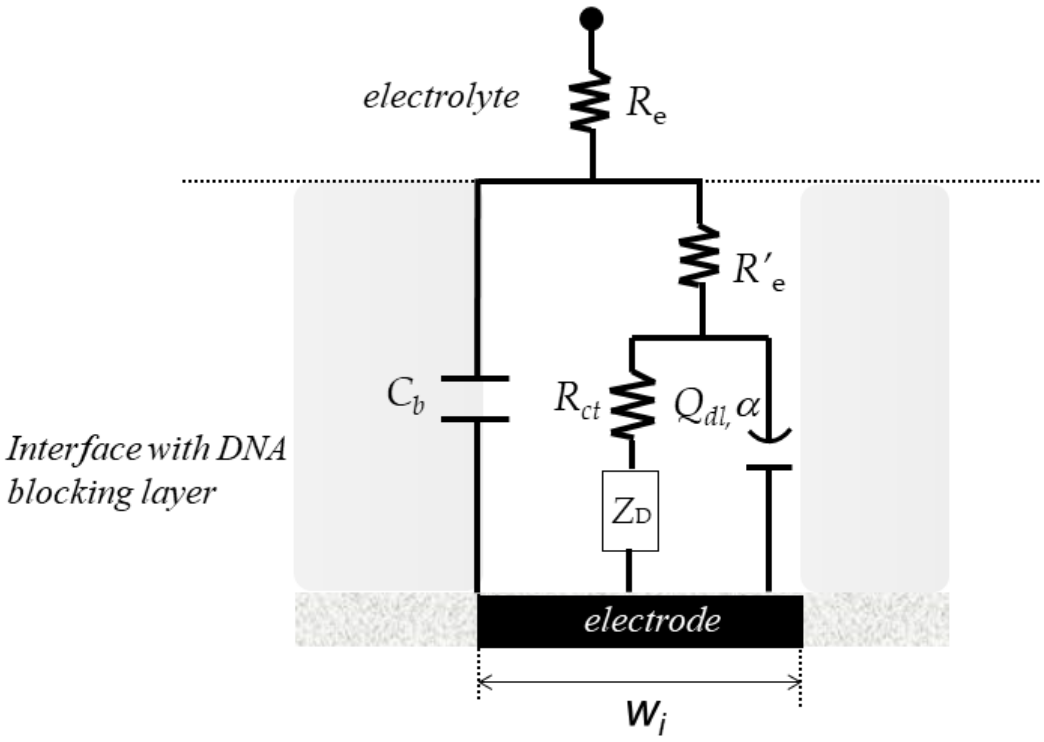

Fig. 5: Electrical equivalent circuit proposed for impedance plots simulation of Au and Pt electrodes partially blocked with a porous DNA monolayer after functionalization with probes or/ and after hybridization with increasing concentrations of targets.

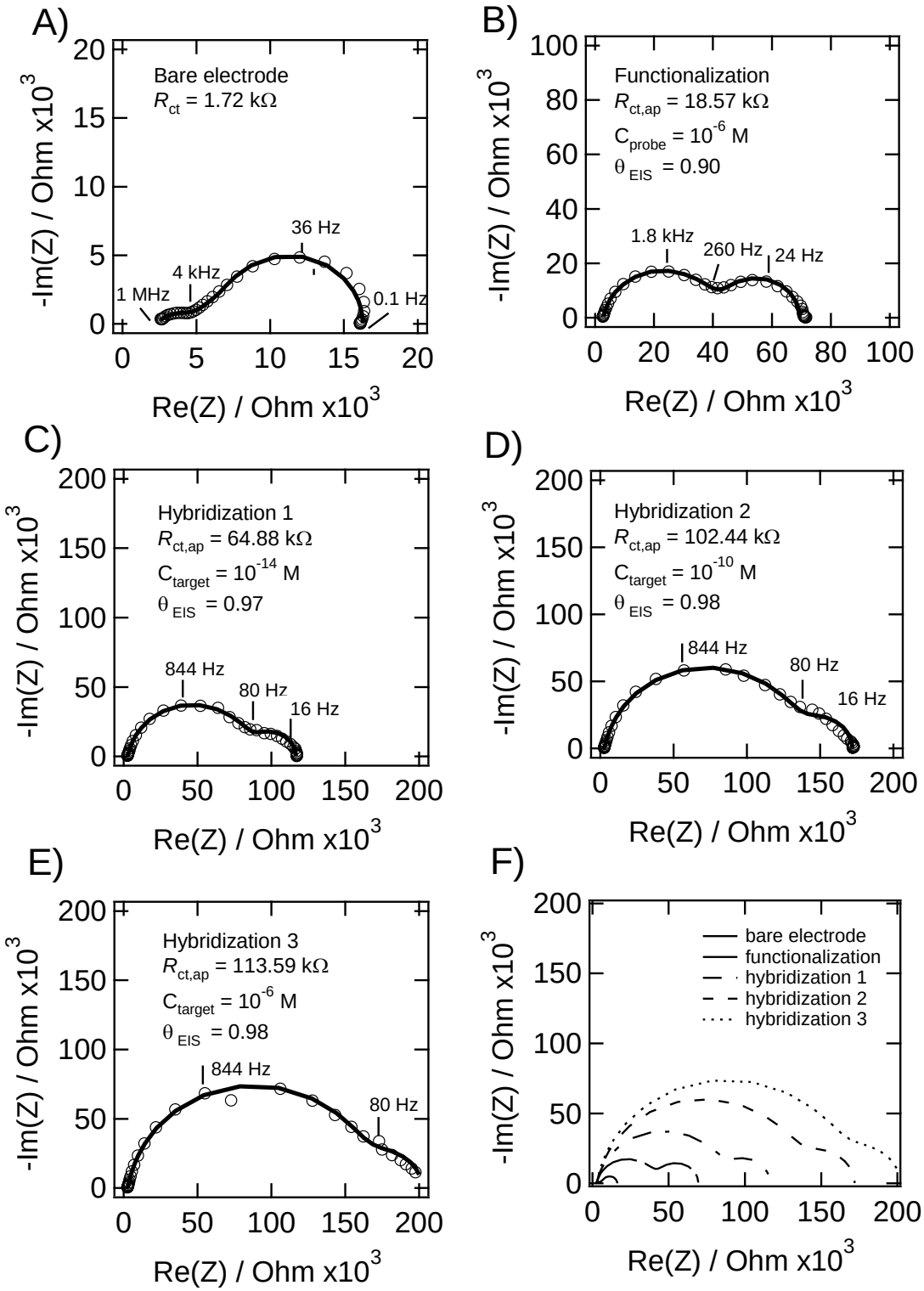

Fig. 6: Experimental (symbols) and simulated (lines) EIS plots on platinum electrode PT1 in solutions containing 20 mM $Fe(CN)_6^{3-}$ and 20 mM $Fe(CN)_6^{4-}$. A) Bare electrode. B) After functionalization with probes. C-E) After hybridization with increasing concentrations of targets. F) Simulated EIS plots in (A-E). See Table S1 for experimental conditions and fitting parameters.

Graphical abstract